ACS OMEGA

Open Access

This article is licensed under CC-BY-NC-ND 4.0

http://pubs.acs.org/journal/acsodf

Article

Study of Cation Distribution and Photocatalytic Activity of Nonthermal Plasma-Modified $NiZnFe_2O_4$ Magnetic Nanocomposites

Muhammad Aqib Busharat, Shazia Shukrullah,* Muhammad Yasin Naz, Yasin Khan, Ahmed Ahmed Ibrahim, Abdulrehman Ali Al-Arainy, and Muhammad Shoaib

Cite This: *ACS Omega* 2024, 9, 14791−14804

Read Online

ACCESS | Metrics & More | Article Recommendations

ABSTRACT: In this study, $NiZnFe_2O_4$ composite was synthesized using a sol−gel route and subjected to nonthermal plasma treatment for tailoring their cations' distribution and physicochemical, magnetic, and photocatalytic properties. Microwave plasma treatment was given to the composites for 60 min in support of postsynthesis sintering at 700 °C for 5 h. X-ray diffraction (XRD) analysis was conducted on pre- and postplasma-modified ferrite composites to identify phase-pure cubic spinel structure and cations' distribution. The cation distributions were measured from the ratio of XRD intensity peaks corresponding to (220), (311), (422) and (440) planes. The intensity ratio of plasma-treated ferrite composites decreased compared to that of pristine composites. The crystallite size and lattice constant were increased on plasma treatment of the composite. The morphological analysis showed nanoflower-like structures of the particles with an increased surface area in the plasma-treated composites. The plasma oxidation and sputtering effects caused a reduction in the nanoflower size. The energy bandgap increased with a decrease in particle size due to plasma treatment. The rhodamine B dye solution was then irradiated with a light source in the presence of the nanocomposites. The dye degradation efficiency of the composite photocatalyst increased from 80 to 96% after plasma treatment.

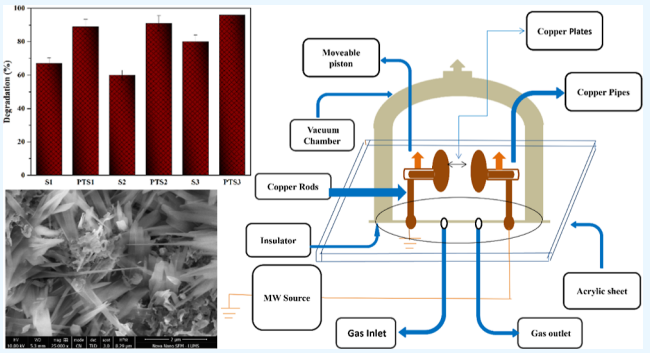

INTRODUCTION

In recent years, magnetic nanoparticles (MNPs) have been investigated for some special characteristics, differentiating them from their bulk counterparts.[1,2] MNPs are also effective as photocatalysts for degrading organic pollutants and as adsorbents for removing heavy metals.[3] MNPs are also easy to separate from the treated solution through filtration, centrifugation, and an external magnetic field. When employed as a photocatalyst, MNPs have the ability to show high photocatalytic performance under the combined action of photocatalytic and magnetic properties. Magnetic photocatalysts also reduce the risk of contamination in reaction mixtures, since they can easily be removed from the mixture through an external magnetic field. A magnetic photocatalyst must be completely removed from the product when it is not compatible with the reactants or when removal of the photocatalyst from the product is required. Other major applications of MNPs include gas sensors,[4] humidity sensors,[5] photocatalysis,[6,7] anode material,[8] inorganic pigments, and removal of heavy metals.[9] The photocatalytic activity of ferrite MNPs can be influenced by morphology, particle size, and synthesis method. The choice of MNPs depends on the specific needs of the dye degradation process and the environmental conditions. The nanoparticles of $ZnFe_2O_4$ and $NiFe_2O_4$ have been reported for photocatalytic degradation of organic dyes. Singh et al.[10] investigated the effect of sintering temperature on structural, magnetic, optical, and photocatalytic traits of $NiCrFeO_4$ ferrites. The band gap of the ferrite photocatalyst was reported in the visible region, making it a suitable candidate for photocatalytic applications. They tested the photocatalytic response of $NiCrFeO_4$ ferrites by degrading rhodamine B (RhB) dye in mild oxidant H_2O_2. It is observed that the photocatalyst prepared using PVA as the fuel exhibited the best photocatalytic activity at all sintering temperatures. The surface area of the photocatalyst, prepared with PVA and urea, decreased over sintering temperature. The photocatalytic activity also decreased over sintering temperature due to a decrease in active surface area. Overall, the dye degradation profiles followed pseudo-first-order kinetics. Das

Received: September 9, 2023
Revised: February 23, 2024
Accepted: March 12, 2024
Published: March 22, 2024

© 2024 The Authors. Published by American Chemical Society

et al.[11] tested catalytic activity of heterogeneous ditopic $ZnFe_2O_4$ for the production of 4*H*-pyrans. The ferrite catalyst provided both acidic and basic functionalities to drive the reaction. Combining Ni and Zn in $NiZnFe_2O_4$ may enhance photocatalytic properties compared to individual ferrite nanoparticles.[8−10] The synergy between Ni and Zn ions could lead to a high charge separation and photocatalytic efficiency.

In ferrite MNPs, microstructures of NiZn ferrites are more sensitive to the applied electromagnetic fields, ferrite composition, sintering conditions, grain size, nature and amount of additives and impurities, and synthesis method.[9,10] There are 32 closely packed oxygen atoms in cubic crystals of spinal magnetic ferrites (MFe_2O, M = Ni, Co, Mg, Mn, Ca, etc.). Out of these 32 sites, only 8 tetrahedra (A) and 16 octahedra (B) sites are engaged in electrical neutrality.[11] Because of the cations' distribution between sites A and B, spinel ferrites comprise three different structures. The cation M^{2+} is located in A-sites and cation Fe^{3+} is located in the B-sites of $(M^{2+})_A[Fe^{3+}Fe^{3+}]_BO_4$ spinel structure.[12] It is observed that M^{2+} cations are found only at B-sites of inverse spinel structures, such as $(Fe^{3+})_A[M^{2+}Fe^{3+}]_BO_4$. On the other hand, Fe^{3+} cations show a uniform distribution among A and B sites in this structure. In a mixed spinel structure, M^{2+} and Fe^{3+} inhabit tetrahedral and octahedral positions randomly, such as $(M^{2+}{}_{1-\delta}\ Fe^{3+}{}_{\delta})_A\ (M^{2+}{}_{\delta}\ Fe^{3+}{}_{2-\delta})_BO_4$.[13] A spinel ferrite structure with an inversion degree of 0 has no Fe^{3+} cations. In contrast, one with an inversion degree of 1 has one Fe^{3+} cation.[14] The physicochemical characteristics of MNPs are significantly influenced by the distribution of cations on their A and B sites, synthesis process and stoichiometry.[15]

The cation distribution in heterogeneous photocatalysts plays an important role in determining their effectiveness for degrading environmental pollutants.[16] The most commonly used photocatalysts for wastewater treatment are ZnO and TiO_2. These are low-cost photocatalysts with reasonably high oxidation capacity, photosensitive properties, bioconsistency, acceptable photocatalytic performance, and chemical stability.[17] However, these photocatalysts exhibit fast recombination of charge carriers in their pure form. The postprocessing recovery of these materials from the solution is also challenging in many cases. The nonmagnetic nature MnO_2, TiO_2, ZnO, ZnS, and so on make it difficult for them to recover from the treated medium and recycle them for multiple operations. This problem can be addressed using MNPs, such as spinel-structured ferrites.[17−20] The spinel ferrites are more efficient and cost-effective than ordinary magnetic materials for performing advanced oxidation processes (AOPs). The MNPs-driven AOPs can be the best alternatives to the adsorption, precipitation, and filtration process.[18] The ferrite AOPs are easy to operate, highly efficient, and environmentally friendly. Photocatalytic processes, commonly used for wastewater treatment, are a type of AOPs. Hydroxyl radicals (•OH) are produced in AOPs nonselectively and in large quantities. Hydrogen peroxide is an oxidizing agent and Fe^{3+}/Fe^{2+} acts as a catalyst to form hydroxyl radicals by interacting with Fe^{3+}/Fe^{2+} ions.[20,21] Besides this, ferrite MNPs can serve as an excellent catalyst support for processes such as Fenton and photo-Fenton reactions. A Fenton process involves the generation of •OH radicals from hydrogen peroxide in the presence of an iron catalyst. The ferrite-based catalyst can enhance the catalytic activity of Fe^{3+}/Fe^{2+} ions iron in a Fenton reaction due to their high surface area and reactivity.[21]

The reactivity and surface properties of MNPs can be enhanced further by treating them with nonthermal plasma discharges.[22] Plasma treatment of MNPs can play a significant role in AOPs for degrading dyes from wastewater. When MNPs are introduced to a plasma discharge, they are exposed to different reactive species. These species interact with their surface and activate the surface sites, create surface defects, generate new functional groups and modify the existing ones.[23] The creation of hydroxyl and carboxyl groups under plasma action acts as binding sites for contaminants, making it easier for MNPs to adsorb and oxidize the pollutants in wastewater. Other than this, the plasma etching effect enhances the surface roughness of nanoparticles, providing a more reactive surface area to accelerate AOPs. In this work, $ZnFe_2O_4$, $NiFe_2O_4$, and $NiZnFe_2O_4$ MNPs were produced using sol−gel method[20−25] and given microwave plasma (MWP) treatment for 60 min to tailor their cations' distribution and photocatalytic properties. The distribution of cations was measured from the intensity ratios of the X-ray diffraction (XRD) peaks for different crystal planes. Pristine and plasma-modified MNPs were used to degrade RhB dye in the wastewater.

MATERIALS AND METHODS

Synthesis of MNPs. The nanoparticles of $ZnFe_2O_4$, $NiFe_2O_4$, and $NiZnFe_2O_4$ ferrites were produced using the sol−gel method. The starting materials were $Zn(NO_3)_2{\cdot}6H_2O$, $Ni(NO_3)_2{\cdot}6H_2O$, and $Fe(NO_3)_3{\cdot}9H_2O$. The initial molar ratio was Ni/Zn/Fe = 1:1:2. The contamination-free synthesis environment was achieved by washing the glassware with deionized water. A solution was prepared by mixing Ni, Zn, and Fe salts with deionized water. Initially, 2.0 g of $Ni(NO_3)_2{\cdot}6H_2O$ and 5.56 g of $Fe(NO_3)_3{\cdot}9H_2O$ were dissolved in deionized water. In the second step, 2.0 g of $Ni(NO_3)_2{\cdot}6H_2O$, 2.05 g of $Zn(NO_3)_2{\cdot}6H_2O$, and 5.56 g of $Fe(NO_3)_3{\cdot}9H_2O$ were dissolved in deionized water. In the third step, 2.05 g of $Zn(NO_3)_2{\cdot}6H_2O$ and 5.56 g of $Fe(NO_3)_3{\cdot}9H_2O$ were dissolved in deionized water. These three solutions were separately placed on magnetic hot plates and stirred for 60 min by maintaining the solution temperature at 80 °C. The ammonia was mixed with the solution dropwise to maintain the pH. When heated further, the sol turned into a gel, which could be settled down if heated continuously. A fine powder was obtained after heating the material for 12 h at 90 °C. A second oven drying process at 90 °C was followed by calcination for 4 h at 700 °C to induce strong magnetic character in MNPs powder. The prepared $NiFe_2O_4$, $ZnFe_2O_4$, and $NiZnFe_2O_4$ MNPs samples were labeled as S1, S2, and S3, respectively. These samples were plasma-modified and relabeled as PTS1, PTS2, and PTS3, respectively.

Plasma Treatment of MNPs. A low-pressure chamber was used to give MWP treatment to S1, S2, and S3 samples of MNPs. Each sample was exposed to MWP of oxygen for 60 min. The low-pressure oxygen plasma species caused cleaning etching and functionalization of MNPs by the introduction of new functional groups on their surface. It is the most practical, economical, and environmentally friendly method for enhancing the reactivity and surface properties of the catalyst. In the MWP setup, a MW source of 1000 W was used to produce oxygen plasma in a vacuum-tight chamber. The setup typically consisted of an MW source, MW shielding, plasma chamber, vacuum system, temperature monitoring system, gauges, sample holder, and MW controller. Figure 1 shows schematically how MWP is used to treat MNPs powder. A boat was

https://doi.org/10.1021/acsomega.3c06883
ACS Omega 2024, 9, 14791−14804

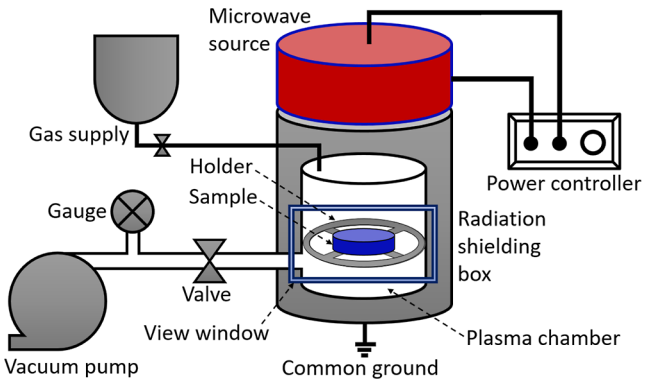

Figure 1. Construction of the MWP setup for the treatment of MNPs.

used to transport the powder to the MWP chamber. A two-stage vacuum pump was used to vacuumize the plasma chamber. Thereafter, the chamber was flushed with precursor gas by adjusting the chamber pressure to the required level. Gas molecules were broken down into plasma species and electromagnetic radiation under MW exposure. The physical, magnetic, and structural properties of the sample were changed due to a reaction between the reactive species and the surface of nanoparticles.[22]

Characterization of MNPs. To investigate the structural properties of MNPs samples, XRD analysis was performed with a Cu K radiation source operated with 43 kV in a Bruker D8 X-ray diffractometer. XRD analysis was conducted on pre- and postplasma-modified ferrite composites to identify phase-pure cubic spinel structure and cations' distribution. SEM 450 field emission electron microscope was employed to produce high-resolution images for the study of surface morphology of the samples. FTIR spectra were obtained between a wavenumber range of 4000 to 500 cm^{-1} to study the functional groups of pristine and MWP-modified MNPs. A vibrating sample magnetometer (VSM) setup with applied fields of ±10 kOe was used to produce magnetic hysteresis of all of the samples. A UV−vis absorption spectrometer was used to

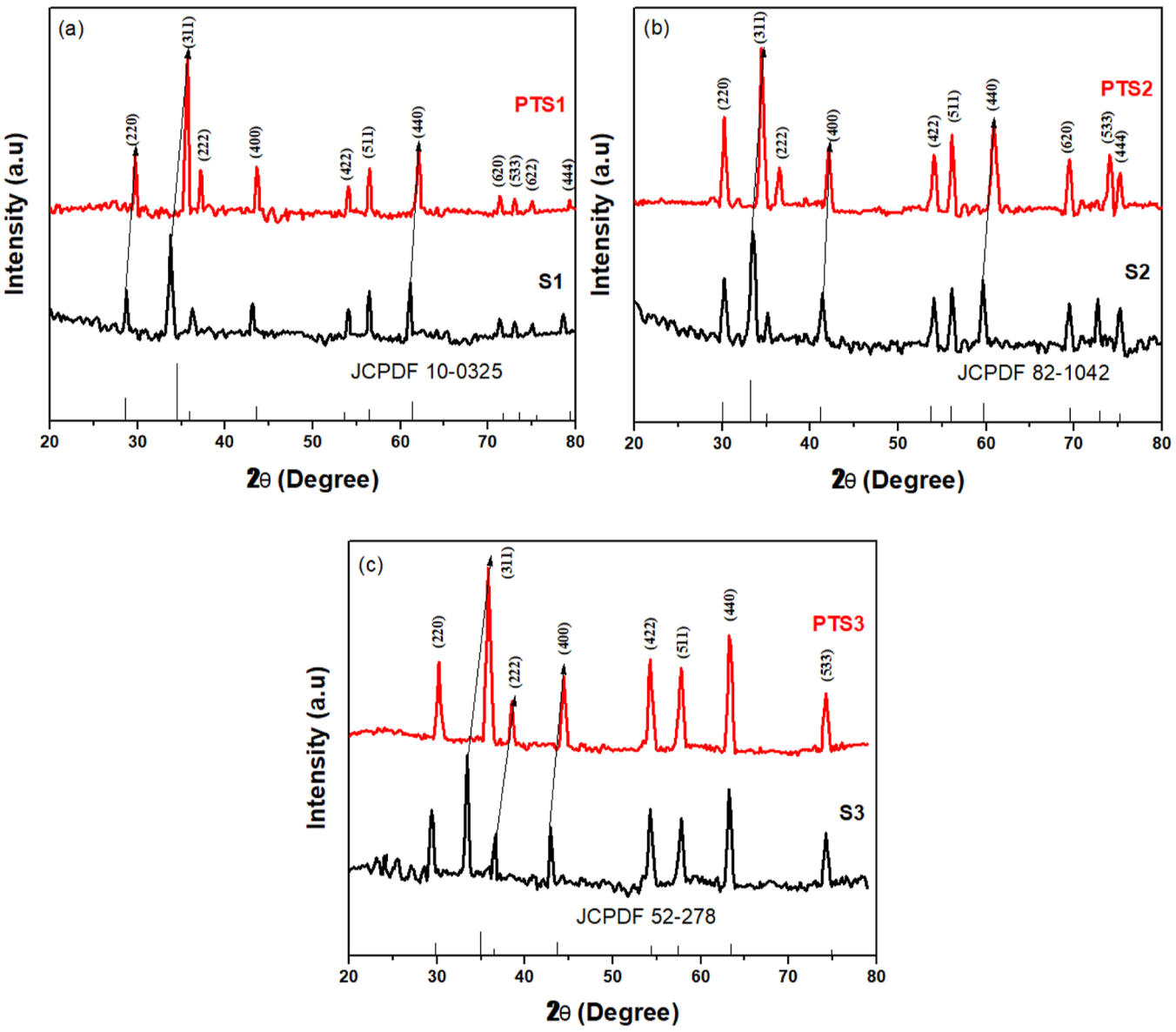

Figure 2. XRD spectra of pristine and plasma-modified MNPs: (a) S1 and PTS1, (b) S2 and PTS2, and (c) S3 and PTS3.

https://doi.org/10.1021/acsomega.3c06883
ACS Omega 2024, 9, 14791−14804

record the optical absorption spectra to examine the band gap energy of the MNPs. A Malvern Zetasizer was used to measure the particle sizes of the pristine and MWP-modified MNPs.

Photocatalytic Dye Degradation. In dye degradation tests, 20 ppm solution of RhB dye was irradiated with a light source in the presence of pristine and MWP-modified MNPs to check their photocatalytic efficiency. An average concentration of 0.04 g of photocatalyst was added to 50 mL of dye solution and placed in the dark for 3 h under continuous stirring before exposing it to the light. We measured the photocatalytic response of MNPs under identical conditions in all dye solutions. About 3 mL of the reaction solution was collected after specific time intervals for UV−vis analysis. The following eq 1 was used to measure the quantity of dye removed each time

$$\text{Degradation of dye (\%)} = \frac{C_0 - C_t}{C_0} \times 100\% \tag{1}$$

where C_0 shows the concentration of dye at $t = 0$, C_t shows the concentration of dye at time t. RhB degradation was used to test the catalytic performance of each MNPs sample since RhB exhibits its absorbance peak at 665 nm.

RESULTS AND DISCUSSION

Structural Properties and Cation Distribution. XRD spectra of both pristine and plasma-exposed MNPs samples are provided in Figure 2. All of the samples formed pure phases due to the diffraction peaks allocated to the spinel structure. XRD peaks provide an estimate of porosity level, crystallite size, lattice constant, and unit cell volume of the nanoparticles. XRD peaks of S1 and PTS1 agreed well with JCPDS card no. 10-0325.[26] XRD peaks of S2 and PTS2 agreed well with JCPDS card no. 82-1042.[27] Similarity, XRD peaks of S3 and PTS3 agreed well with JCPDS card no. 52-278.[28] The matched data of the ferrite MNPs confirmed the FCC structure. XRD peaks of the S1 and PTS1 samples revealed (220), (311), (222), (400), (422), (511), (440), (620), (533), (622), and (444) planes in its crystal structure.[26] XRD peaks of the S2 and PTS2 samples revealed (220), (311), (222), (400), (422), (511), (440), (620), (533), and (444) planes in its crystal structure.[27] XRD peaks of the S3 and PTS3 samples revealed (220), (311), (222), (400), (422), (511), (440), and (533) planes in their crystal structure.[28] A seamless crystal arrangement and pure phase formation can be observed in all intermediate configurations, because there are no impurity peaks in the spectra. Plasma-treated samples also showed the same peaks as the pristine samples in the XRD spectra. The plasma treatment did not alter the major phases of the MNPs. The XRD peaks in all samples were shifted toward higher angles, as shown in Figure 2. Due to an inverse relationship between lattice parameters and diffraction angles, this shift results in a drop in lattice parameters. The lattice parameter of the S3 sample decreased compared to that of the S2 sample because the smaller ionic radius of Ni^{2+} at tetrahedral sites was replaced by a larger ionic radius of Zn^{2+}, resulting in a decrease in the lattice parameter value. Equation 2 was used to calculate the lattice parameters "a" of the pristine and MWP-modified MNPs.

$$a = d\sqrt{h^2 + k^2 + l^2} \tag{2}$$

Crystallization of MNPs was measured using a peak with the highest intensity for the (311) plane. The crystallite size can be obtained from XRD data using Scherrer's formula in eq 3.[23,24]

$$L = \frac{0.89\lambda}{\beta \cos\theta} \tag{3}$$

where λ is the wavelength of incident X-rays, θ is the Bragg angle, β is FWHM, and L is the grain size. The unit cell volume and lattice parameters were used in eq 4 to estimate X-ray density as

$$\rho_x = \frac{NM}{VN_A} \tag{4}$$

Avogadro's number is indicated by N_A. Formula units and molecular weights are represented by N and M, respectively. The following eq 5 was used to estimate the bulk density of MNPs

$$\rho_b = \frac{M}{V} \tag{5}$$

where, pellet volume and mass are given by V and M, respectively. By having the above information, one can determine the porosity of the MNPs from eq 6.[23]

$$\text{Porosity} = \left(1 - \frac{\rho_b}{\rho_x}\right) \times 100\% \tag{6}$$

A Bertaut method was used to obtain information on the distribution of cations from XRD data by comparing the observed intensity ratios with the calculated intensity ratios after selecting some pairs of reflections, as shown in eq 7.[24]

$$\frac{I_{hkl}^{obs}}{I_{h'k'l'}^{obs}} \propto \frac{I_{hkl}^{cal}}{I_{h'k'l'}^{cal}} \tag{7}$$

The X-ray intensity for different planes (I_{hkl}) was calculated using eq 8

$$I_{hkl} = |F|_{hkl}^2 P \cdot \text{Lp} \tag{8}$$

The Bragg's diffraction angle was used to determine the structural factor F, while P is a multiplicity factor determined by multiplicity and Lp is a Lorenz polarization factor determined by the Lorenz polarization angle in eq 9.

$$\text{Lp} = 1 + \cos^2 2\theta / \sin^2\theta \cos 2\theta \tag{9}$$

XRD patterns of spinel structures showed peaks with intensity ratios indicative of cation distribution, such as I_{220}/I_{311} and I_{422}/I_{440}.[25] Because absorption and temperature factors are not considered effective when calculating the relative intensity at room temperatures. Using eq 10, we can calculate the theoretical lattice parameter.

$$a_{th} = \frac{8}{3\sqrt{3}}[(r_A + R_o) + \sqrt{3}(r_A + R_o)] \tag{10}$$

where R_o is the radius of the oxygen ions (1.32 Å), r_A is the radius of tetrahedral site, and r_B is the radius of octahedral site. Both r_A and r_B were calculated using eqs 11 and 12.[24]

$$r_A = (1 - x) r_{NiZn}{}^{2+} + x r_{Fe}{}^{3+} \tag{11}$$

$$r_B = \frac{1}{2}[x r_{NiZn}{}^{2+} + (2 - x) r_{Fe}{}^{3+}] \tag{12}$$

https://doi.org/10.1021/acsomega.3c06883
ACS Omega 2024, 9, 14791−14804

Table 1. XRD Data and Cation Distribution of Pristine and Plasma-Modified MNPs

parameter	PTS1	S1	PTS2	S2	PTS3	S3
lattice constant (Å)	8.39 ± 0.25	8.34 ± 0.5	8.21 ± 0.5	8.19 ± 0.5	8.42 ± 0.5	8.39 ± 0.5
crystallite size (nm)	35.21 ± 2	31.21 ± 2.3	32.43 ± 2	25.40 ± 2	56 ± 2	47 ± 2
volume of the unit cell (A^3)	579.22 ± 8.1	575.43 ± 7.6	592.32 ± 4.0	589.51 ± 7.3	599.25 ± 5.9	595.56 ± 5.2
bulk density (g/cm^3)	0.98 ± 0.01	0.93 ± 0.01	5.71 ± 0.01	5.27 ± 0.01	5.60 ± 0.01	5.11 ± 0.01
porosity (%)	2.32	2.21	2.5	2.43	2.76	2.67
			Cation Distribution			
r_A (Å)	0.8685 ± 0.01	0.8599 ± 0.01	0.8595 ± 0.01	0.8483 ± 0.01	0.8790 ± 0.01	0.8634 ± 0.01
r_B (Å)	0.6329 ± 0.01	0.6289 ± 0.01	0.6287 ± 0.01	0.6211 ± 0.01	0.6433 ± 0.01	0.6299 ± 0.01
a_{th} (Å)	8.38 ± 0.5	8.34 ± 0.5	8.21 ± 0.5	8.19 ± 0.5	8.42 ± 0.5	8.39 ± 0.5
a_{exp} (Å)	8.39 ± 0.5	8.35 ± 0.5	8.21 ± 0.5	8.19 ± 0.5	8.41 ± 0.5	8.40 ± 0.5
I_{220}/I_{311}	obs cal	obs cal	obs cal	obs cal	obs cal	obs cal
	1.24 1.27	1.28 1.30	1.21 1.19	1.24 1.20	1.12 1.10	1.15 1.13
I_{422}/I_{440}	obs cal	obs cal	obs cal	obs cal	obs cal	obs cal
	0.50 0.56	0.60 0.63	0.43 0.45	0.47 0.49	0.40 0.38	0.41 0.38

Table 1 provides information on the calculated tetrahedral radius, octahedral radius, theoretical a_{th}, and experimental a_{exp} lattice parameters. A decrease in "r_A" was observed, whereas an increase in "r_B" was observed after plasma treatment. Calculations based on the X-ray intensity indirectly confirm the cation distribution obtained from a_{th} and a_{exp}. The experimental lattice constant, crystallite size, unit cell volume, bulk density, porosity, and cation distribution are all reported in Table 1.

FTIR Analysis of MNPs. FTIR analysis was performed to better understand the bond formation and site formation within octahedral and tetrahedral sites of MNPs. These bonds and sites play an important role in defining the electric and magnetic properties of the MNPs. FTIR spectra of pristine and MWP-modified nanoparticles is shown in Figure 3. In the

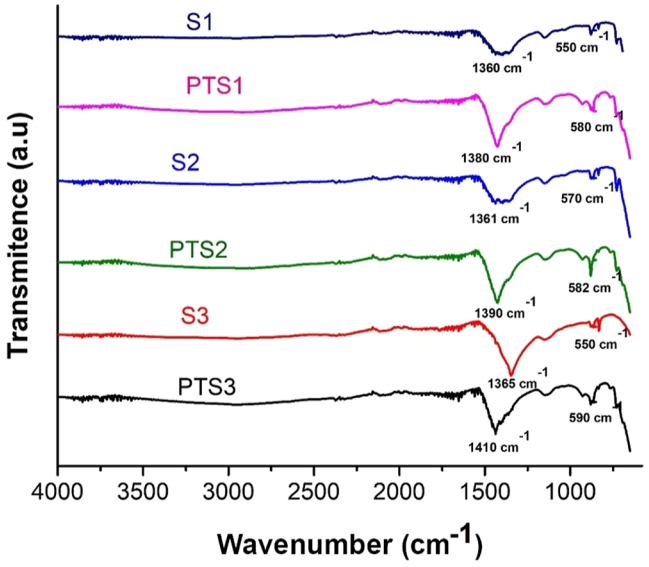

Figure 3. FTIR spectra of pristine and plasma-modified MNPs.

spinel structure, there are two main bonds between oxygen (O) and metal (M), which are found in octahedral and tetrahedral sites. There is a strong relationship between the physical properties of nanoparticles and the occupancy of different kinds of atoms at the tetrahedral and octahedral sites. There is a much greater tendency for Zn atoms to occupy tetrahedral sites, whereas Ni atoms are able to occupy either octahedral or tetrahedral sites.[29] In FTIR spectra, spinel ferrites are typically characterized by a wavenumber between 400 and 4000 cm^{-1}. Strong absorption peaks near 1360 and 1430 cm^{-1} indicate that many OH radicals existed in both plasma-treated and untreated samples. Two very strong absorption peaks between 550 and 670 cm^{-1} should be caused by the stretching vibration of Zn−O and Ni−O bonds.[30]

Morphology and Size Analysis. The morphology of the pristine and plasma-modified MNPs was examined through SEM analysis. SEM images showed more likely needled nanoflower structures of pristine MNPs. Some lumps of nanoparticles of different shapes were agglomerated within the forest of nanoflowers. The S3 sample in Figure 4 showed more agglomeration of nanoparticles within the forest of nanoflowers compared to S1 and S2 samples. It reveals that the growth of nanoflower-like structures in the NiZn ferrite composite was high compared to pure Ni and Zn ferrites. The morphology of the MNPs became clearer and more defined after MWP exposure. The plasma reactive ions and radicals etched away the undesired contaminants, materials and oxide layers from the particle surface.[23,31] Plasma exposure also introduces new functional groups onto the particle surface by reacting with surface atoms and molecules and forming covalent bonds and functional moieties. The change in shape or rearrangement of the particle shapes during MWP exposure might be due to the breaking of aggregated or agglomerated nanoparticles. The plasma species provide the necessary energy to overcome the attractive forces between the nanoparticles.[30,32,33]

The nanostructures become more defined and dispersed under weak attractive forces between them. The selective oxidation and reduction of certain surface groups are also possible, which change their electronic and chemical properties. The PTS1 and PTS2 did not show even a single nanoparticle or cluster other than needled nanoflowers, showing well-defined shapes of the MNPs. The PTS3 sample showed reduced agglomeration and clustering of nanoparticles compared to S3 samples, which shows the pronounced effect of plasma treatment on the purity and structural properties of the MNPs. The sharpness of the nanoflower boundaries also decreased slightly during plasma treatment due to the etching of the surface, breakdown of agglomerates, and oxidation of the surface. The needle length of the pristine samples ranged from 400 to 600 nm, which was reduced to 300−500 nm after MWP modification. SEM images clearly showed that nanoflowers are large in shape before plasma treatment and split into small

https://doi.org/10.1021/acsomega.3c06883
ACS Omega 2024, 9, 14791−14804

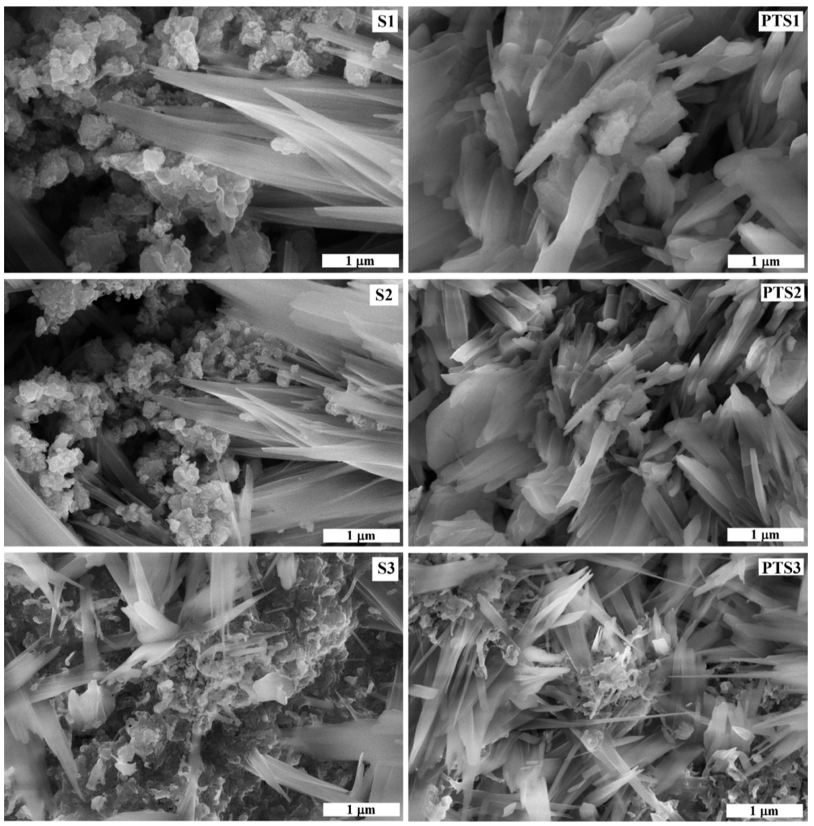

Figure 4. SEM illustration of pristine and MWP-modified MNPs.

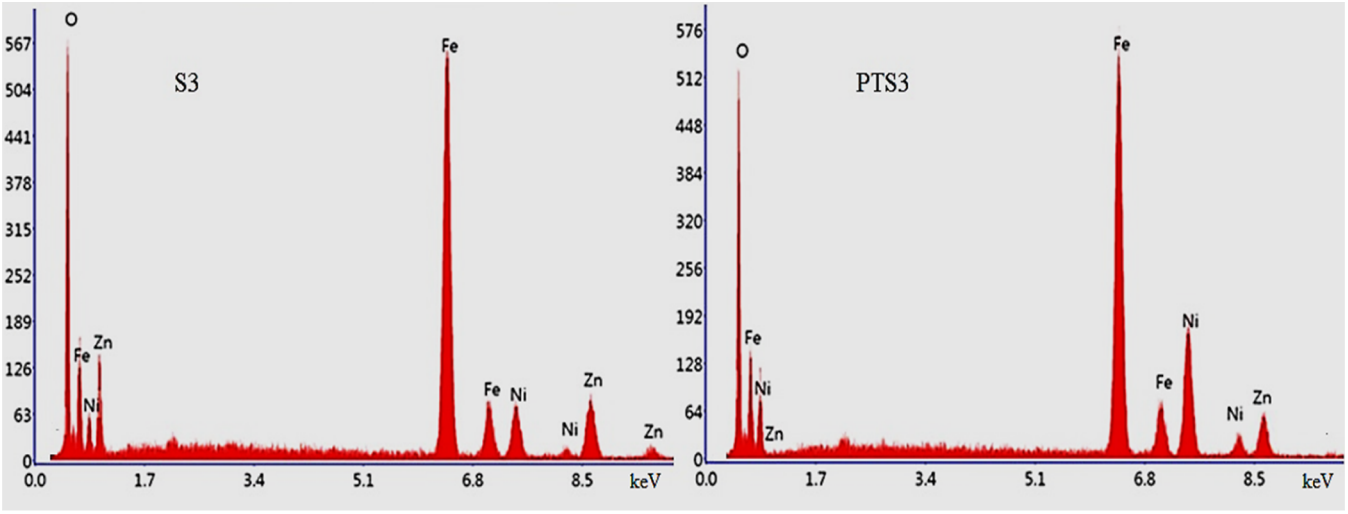

Figure 5. EDX spectra of pristine and MWP-modified MNPs.

nanoflowers after plasma treatment. The surface atoms receive energy from the plasma species. The sputtering phenomenon during plasma exposure causes these surface atoms to excite and leave the surface. A porous surface was also observed on the untreated clusters. By delivering energy to overcome the attraction forces between particles, plasma treatment can also aid in breaking up agglomerates or clumps of nanoparticles. This improves the dispersion and stability of the nanoparticles in solution. This is useful for catalytic applications or for changing electrical behavior.

Figure 5 shows a typical EDX spectrum of pristine and MWP-modified sample PTS3 with both Ni and Zn in the formulation. The elemental compositions of the pristine and treated samples, calculated from EDX spectra, are shown in Table 2. The oxygen content of all samples slightly increased after MWP treatment due to oxidation of the nanoparticles in the oxygen-rich plasma environment. Oxidation typically involves the addition of oxygen to a substance.[31] When MNPs undergo oxidation in the presence of oxygen and other oxidizing agents, there are possible changes in their elemental compositions and properties. Some changes can occur in the oxidation state of the metal ions in the nanoparticle structure due to plasma-driven oxidation. For example, in Fe_2O_3, iron can exist in Fe^{3+} oxidation states. Additional oxides may form

https://doi.org/10.1021/acsomega.3c06883
ACS Omega 2024, 9, 14791−14804

Table 2. Elemental Composition of Pristine and MWP-Modified MNPs

	weight (%)					
element	S1	PTS1	S2	PTS2	S3	PTS3
Ni K	14.20	13.64			11.15	09.36
Zn K			16.18	15.25	09.56	10.11
Fe K	30.10	28.91	34.32	33.05	33.27	32.61
O K	55.70	57.45	49.50	51.70	46.02	47.92
total	100	100	100	100	100	100

on the surface or within the structure of the nanoparticles. For instance, Fe_3O_4 or other oxides may appear to alter the original elemental composition.

The particle size and zeta potential of MNPs was measured in a suspension with Zetasizer. A dynamic light scattering method was used to measure the particle size from the fluctuations in light scattering caused by the Brownian motion of the nanoparticles. An intensity autocorrelation function was used to calculate the hydrodynamic diameter of the nanoparticles. The mean particle size was then used to determine the active surface area of the nanoparticles. The polydispersity index was also checked to study the distribution width of the nanoparticles. The particle size distribution of pristine and MWP-modified MNPs is given in Figure 6. The hydrodynamic diameter of the S1 sample was measured at about 67 nm, which was reduced to 52 nm after plasma exposure. Similarly, the hydrodynamic diameter of both S2 and S3 samples was

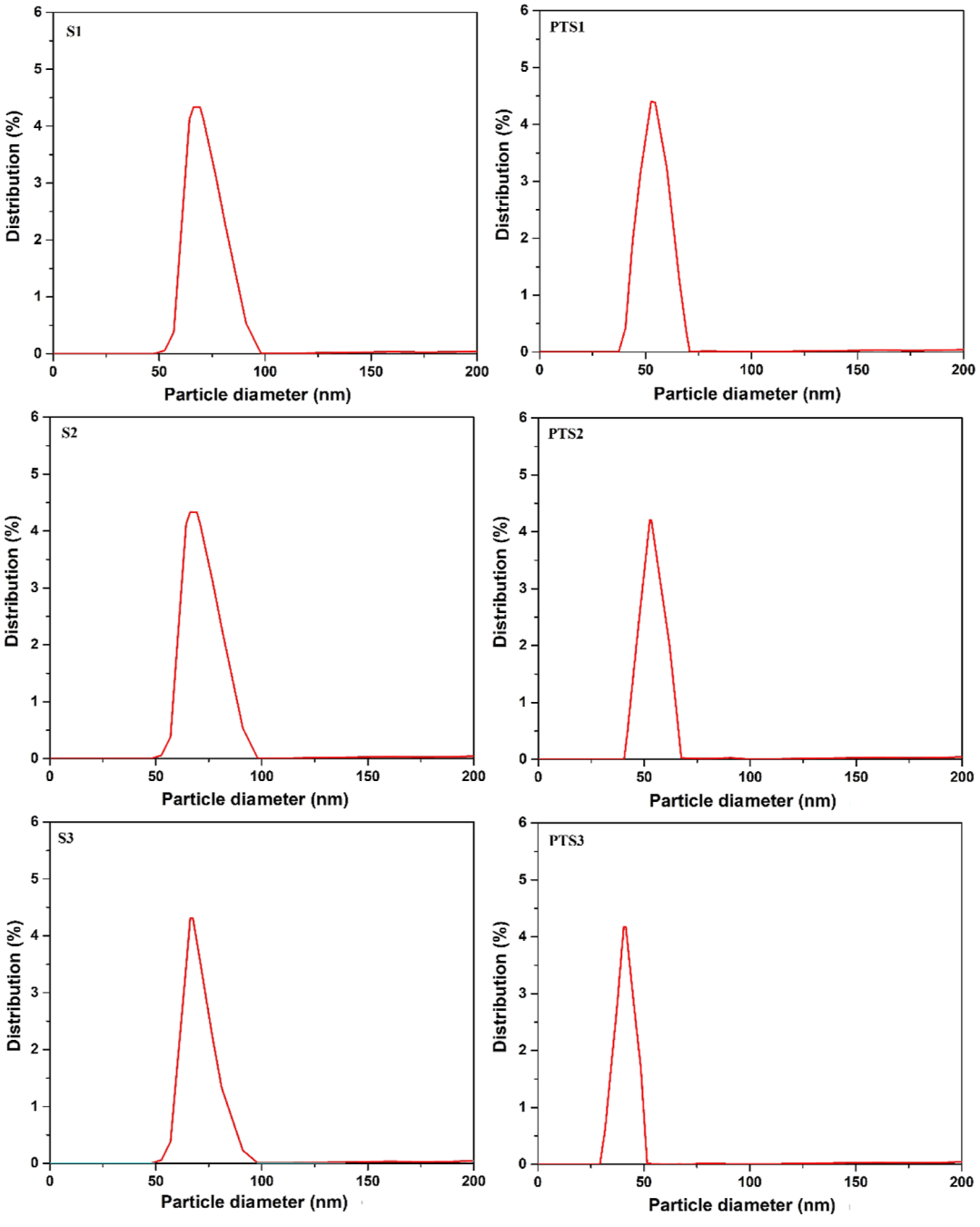

Figure 6. Hydrodynamic diameter of the pristine and MWP-modified MNPs.

https://doi.org/10.1021/acsomega.3c06883
ACS Omega 2024, 9, 14791−14804

measured to be about 65 nm, which was reduced to 51 and 40 nm, respectively, after plasma treatment. The plasma exposure showed a notable effect on the size. PST 3 sample showed the smallest diameter among all the samples. The reduction in size with plasma exposure reflects an increase in the active surface area of the MNPs. The high active surface area supports the photocatalytic application of these nanoparticles.

BET Surface Area Analysis. Figure 7 reports nitrogen adsorption−desorption isotherms of the S3 and PTS3 samples.

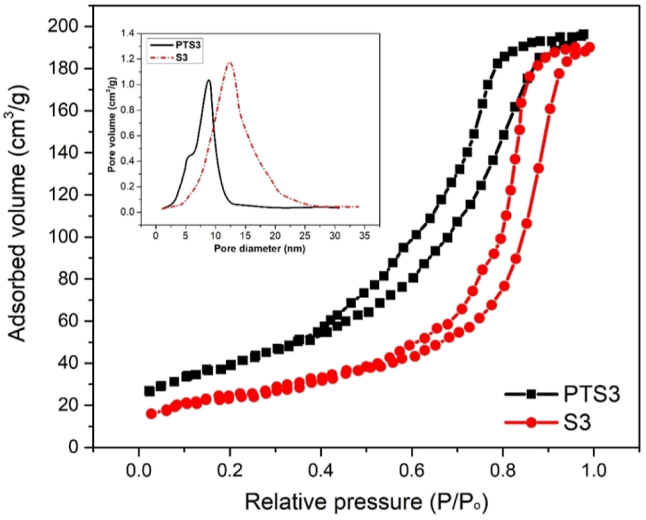

Figure 7. Nitrogen adsorption−desorption isotherms of the S3 and PTS3 samples.

The inset shows the pore volume histogram over the pore diameter. Both S3 and PTS3 samples revealed a mesoporous signature since pore size remained below 50 nm. The nitrogen isotherms showed good morphological properties since both mesoporous samples have high pore volumes. The adsorption isotherms matched with type IV hysteresis loop, showing the mesoporous nature of the samples. The adsorption−desorption branches of the isotherms are slightly different, suggesting relatively wider pore size distribution. Mesopores are typically assigned the diameter range of 2−50 nm. The BJH model analysis confirmed the mean pore size of the tested samples in the mesopore range. The pore volume histogram follows the Gaussian distribution. Table 3 provides a statistical analysis of the pore size, volume, and surface area. The mean pore size was measured about 12.56 and 8.76 nm for S3 and PTS3 samples, respectively. Similarly, the minimum and maximum pore size of the S3 sample was measured about 1.05 and 33.92 nm, respectively. The PTS3 sample showed the minimum and maximum pore sizes of 1.19 and 30.73 nm, respectively. The pore volume of S3 was calculated to be about 0.364 cm^3/g, which was slightly higher than the pore volume of PTS3 (0.329 cm^3/g). However, PTS3 showed a significantly larger surface area of 150.3 m^2/g compared to 115.9 m^2/g of the S3 sample. The large surface area of the plasma processed samples reflects their high photocatalytic activity for degradation of the organic molecules.

Table 3. Statistical Analysis of the Pore Size, Volume, and Surface Area of S3 and PTS3 Samples

sample	mean pore size (nm)	minimum pore size (nm)	maximum pore size (nm)
S3	12.56	1.05	33.93
PTS3	8.76	1.19	30.73
sample	mean pore volume (cm^3/g)	minimum pore volume (cm^3/g)	maximum pore volume (cm^3/g)
S3	0.364	0.027	1.22
PTS3	0.329	0.031	1.05
sample	mean surface area (m^2/g)	minimum surface area (m^2/g)	maximum surface area (m^2/g)
S3	115.9	101.5	143.3
PTS3	150.3	103.3	136.7

VSM Analysis of MNPs. The magnetic properties of magnetic photocatalysts are important for separation from the treated solution for stability testing and recycling. The magnetic properties can be improved through various additives and synthesis methods.[34] This study deals with plasma treatment of MNPs to enhance their magnetic properties. This study specifically examined how plasma treatment affects the magnetic properties of Ni, Zn, and NiZn ferrite nanoparticles. It is important to have a pure phase and a high density in soft ferrites to achieve high saturation magnetization.[35] Both pristine and MWP-modified MNPs showed similar ferromagnetic behavior. However, the saturation magnetization of MNPs increased after plasma exposure, as shown in the M−H curves in Figure 8. In Table 4, PTS3

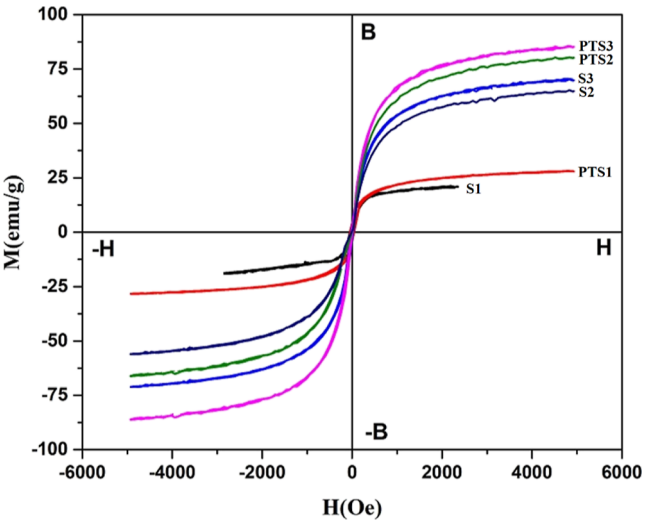

Figure 8. VSM profiles of pristine and MWP-modified MNPs.

samples showed increased M_s, H_c, and M_r values after plasma treatment, indicating that the nanoparticles transformed into hard ferromagnets. As the grain size increases, domain walls within grains increase in number. It requires more energy to magnetize and demagnetize a domain wall than to rotate a domain. As grain size increases, domain walls contribute more

Table 4. Magnetic Parameters of Pristine and MWP-Modified MNPs

sample	M_s (emu/g)	M_r (emu/g)	$R_s = M_r/M_s$	H_c (kOe)
S1	47.5 ± 1	22.12 ± 1	0.47	0.019 ± 0.001
PTS1	58.9 ± 1	32.23 ± 1	0.54	0.038 ± 0.001
S2	31.22 ± 1	17.99 ± 1	0.57	0.011 ± 0.001
PTS2	48.71 ± 1	28.99 ± 1	0.59	0.027 ± 0.001
S3	33.9 ± 1	19.76 ± 1	0.58	0.012 ± 0.001
PTS3	52.76 ± 1	30.52 ± 1	0.67	0.030 ± 0.001

https://doi.org/10.1021/acsomega.3c06883
ACS Omega 2024, 9, 14791−14804

to magnetization and demagnetization than domain rotation.[36] Other possible explanations for the increased M_s, H_c, and M_r values are the weaker superexchange mechanism, including lattice defects and random spin orientation.

UV Analysis of MNPs. The optical behavior of MNPs was studied by using UV−vis analysis. The band gap of each sample was calculated from the respective UV−vis spectrum in Figure 9. Tauc's eq 13 can be used to calculate the energy of the band gap from the absorption profiles as[37,38]

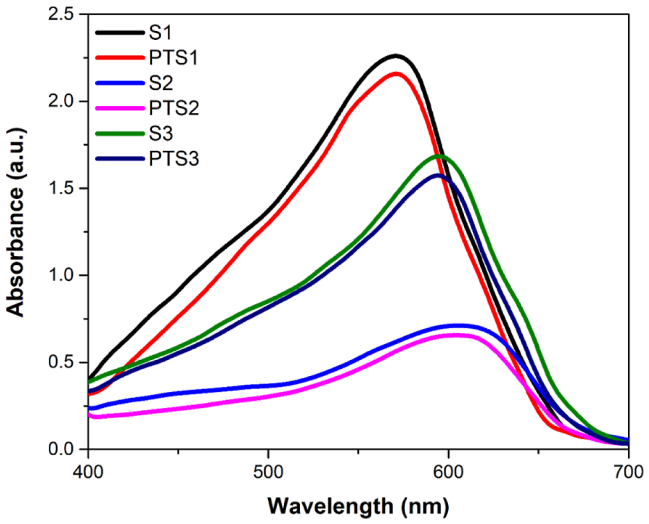

Figure 9. UV absorbance spectra of pristine and MWP-modified MNPs.

$$\alpha = \frac{A}{h\lambda}(h\nu - E_g)^{1/2} \quad (13)$$

where α stands for absorption coefficient, $h\nu$ for photon energy, E_g for optical band gap, and A is a constant.

As shown in Figure 10, the band gap of the S1 sample was calculated as 2.16 eV, which increased to 2.21 eV after plasma exposure. The band gap of S2 sample was calculated as 2.07 eV, which increased to 2.19 eV after plasma exposure. Similarly, the band gap energy of S3 sample increased from 1.88 to 1.98 eV after plasma exposure for 60 min. An increase in band gap is attributed to a decrease in particle size and aggregation due to plasma treatment. Overall, S3 and PST3 samples showed lower band gaps than other pristine and plasma-modified MNP samples.[30,31]

Photoluminescence Analysis. Photoluminescence (PL) spectroscopy was used to study the oxygen vacancies and defects as well as how efficiently charge carriers are trapped and transferred. An explanation of the relationship between the PL spectrum and photochemical activity can be derived from the fact that semiconductors have a band gap energy that is higher than or equal to the excited energy in the PL. Figure 11 shows the PL spectra of optimal sample S3 before and after plasma treatment. $NiZnFe_2O_4$ ferrite is not typically known for its strong PL properties. A characteristic emission at around 428 nm for both samples is characteristic of a near-band-edge emission. As a result of excitonic recombination between electrons in a single oxygen vacancy and the photogenerated hole in the valence band, both samples exhibit a broad visible emission band centered at 428 nm.[39] There is also a possibility that this band is caused by Fe^{3+} ions at octahedral sites and Zn^{2+}, Ni^{2+} ions at tetrahedral sites. At 485 nm, some weak emission bands were observed, which are attributed to oxygen vacancies, causing green emissions. PL intensity peak at a wavelength of 428 nm suggests that the sample emits light in the visible range, typically blue or violet light. However, it is important to note that MNPs such as $NiZnFe_2O_4$ are primarily known for their magnetic properties and are not typically associated with strong PL emissions, especially at that precise wavelength.

Photocatalytic Activity of MNPs. The important factors explaining the photocatalytic activity of the tested MNPs are particle size, reactive surface area and availability of active sites.[39] The degradation of dye with time is reported in Figure 12, showing the rate of dye degradation with the passage of time. As time passes, the degradation of the dyes progresses at different rates. The duration of exposure plays a significant role in determining the overall degradation rate. The control showed roughly 4% degradation of dye after 30 min due to plasma induced reactive species on the fabric surface. No further change in degradation is observed over time after 30 min. The pristine samples initially show a proportionally increasing degradation trend, and then degradation slightly slows down after 50 min on the other hand, the MWP treated samples show a proportionally increasing trend even after 50 min, revealing better catalytic performance compared to pristine samples.

The percentage degradation of RhB dye with pristine and MWP-modified MNPs after 90 min of light exposure is reported in Figure 13. The pristine S1, S2, and S3 samples showed degradation efficiency of 67, 70, and 60%, respectively after 90 min. The degradation efficiency of dye without a catalyst is 4% only. The photocatalytic activity increased after MWP treatment. The plasma-modified PTS1, PTS3, and PTS3 samples showed degradation efficiency of 90, 93, and 98%, respectively, after 90 min. The high reactive surface area, small particle size, typical nanoflower-like structures and formation of functional groups during MWP treatment were the key contributors to the improved photocatalytic activity of the tested MNPs. The percentage degradation efficiency was calculated using eq 14

$$\text{Degradation of dye (\%)} = \frac{C_0 - C_t}{C_0} \times 100\% \quad (14)$$

Photocatalytic dye degradation is more effective with materials with a high specific surface area. Particle size decreases with increasing surface area.[31] The electron−hole recombination rate in single metal ferrites is also high compared to that in composite ferrites. So a large number of electron−hole pairs recombine without contributing to degradation activity. The creation of electron−hole pairs depends on the light absorption characteristics of the photocatalyst. Increased surface area makes it easier to absorb photons, generating more electron−hole pairs that are available for oxidation and reduction reactions.

Table 5 shows a comparison of this work with the published literature. Nam and Boo[40] produced ZnO photocatalyst through the spray pyrolysis method and gave oxygen plasma treatment to improve its photocatalytic activity. The degradation of methylene blue dye increased from 50 to 60% due to plasma treatment. Naz et al.[22] used the assisted sol−gel method to produce $MnFe_2O_4$ MNPs for photocatalytic degradation of dyes. They provided postsynthesis MWP

https://doi.org/10.1021/acsomega.3c06883
ACS Omega 2024, 9, 14791−14804

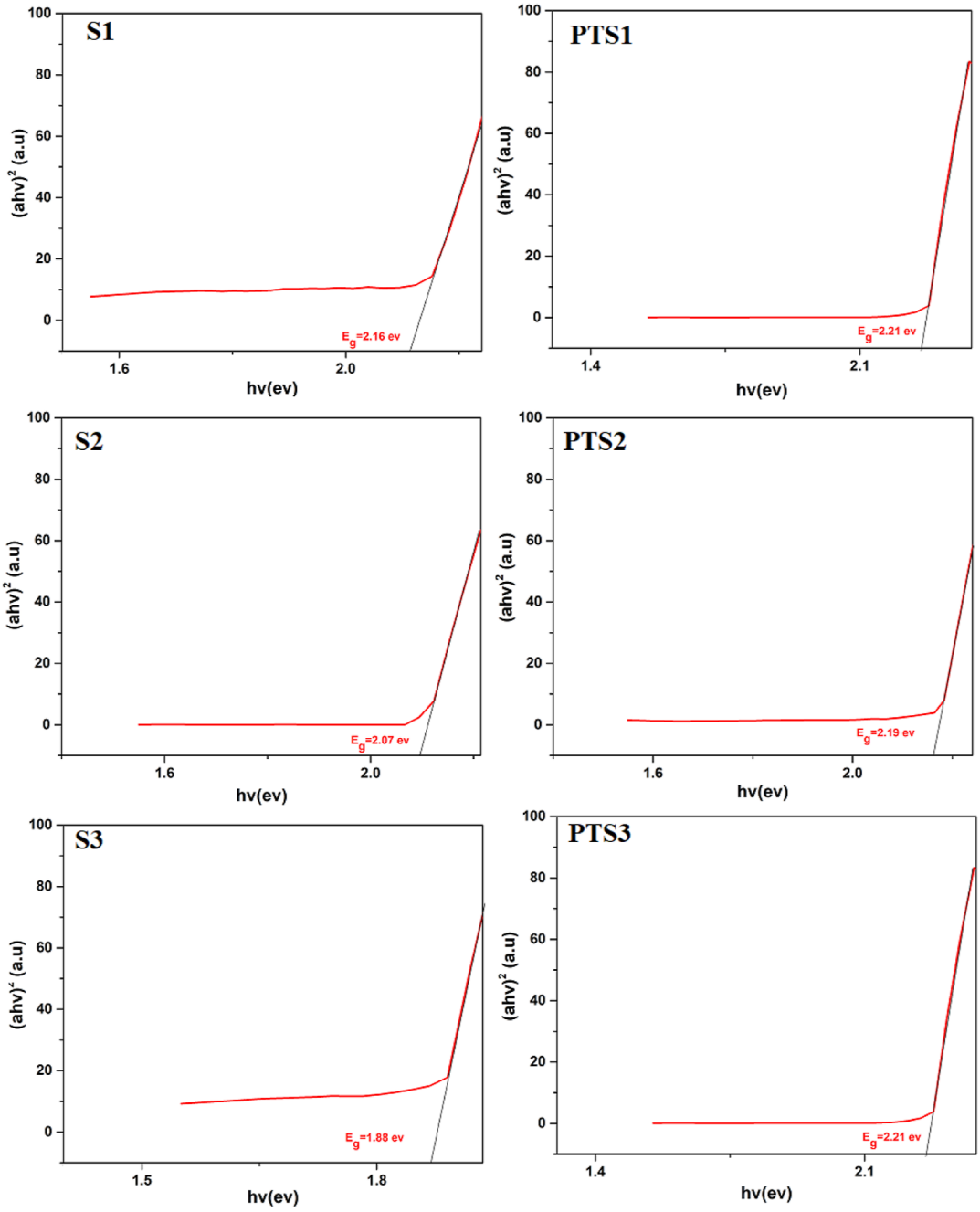

Figure 10. Tauc's plot of pristine and MWP-modified MNPs.

treatment to the ferrite nanoparticles. The effect of plasma treatment on the methylene blue dye was checked. The degradation efficiency increased from 74 to 91% with the MWP treatment of MNPs. A notable increase in efficiency of the photocatalyst was attributed to the removal of impurities, surface activation, and creation of functional groups on the catalyst surface during MWP treatment. Pandiyaraj et al.[41] plasma functionalized Cu−TiO_2 nanoparticles and studied their photocatalytic activity. The dye degradation efficiency increased from 76 to 85% after atmospheric pressure plasma treatment of Cu−TiO_2 nanoparticles. Zolfaghari et al.[42] modified immobilized rutile nanoparticles with low-pressure plasma to test their photocatalytic activity. However, no change in the photocatalytic activity was observed in their work.

Das et al.[43] produced Mn−ZnO magnetic semiconductor nanoparticles through a thermal plasma synthesis process. These nanoparticles were used for the degradation of the methylene blue dye. The degradation efficiency of the plasma-produced nanoparticles was reported to be about 95%. Similarly, Khaledian et al.[44] degraded organic dyes using immobilized titanium dioxide nanoparticles. They reported 72% degradation efficiency with both pristine and plasma modified nanoparticles. Atrak et al.[45] degraded direct blue dye using composite ferrite nanoparticles with a degradation efficiency of 88%. Nguyen et al.[46] used the solution combustion method to produce $MgFe_2O_4$ MNPs for degradation of dyes. They reported a maximum efficiency of 69% against methylene blue dye. Finally, Lassoued et al.[47] produced $NiAlFe_2O_4$ through the coprecipitation method and

https://doi.org/10.1021/acsomega.3c06883
ACS Omega 2024, 9, 14791−14804

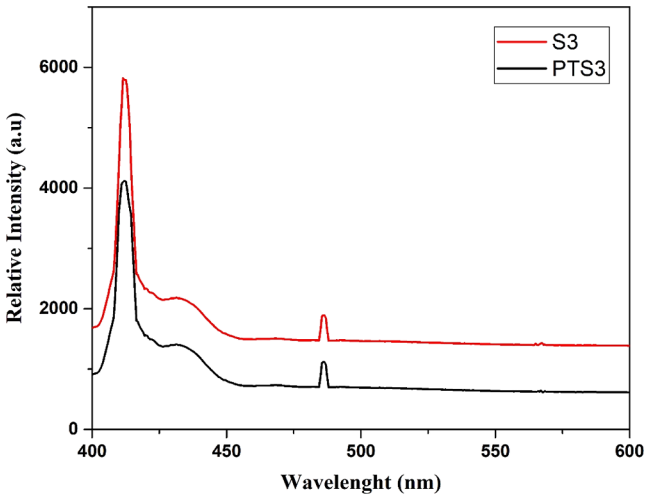

Figure 11. PL spectra of using pristine and MWP-modified MNPs.

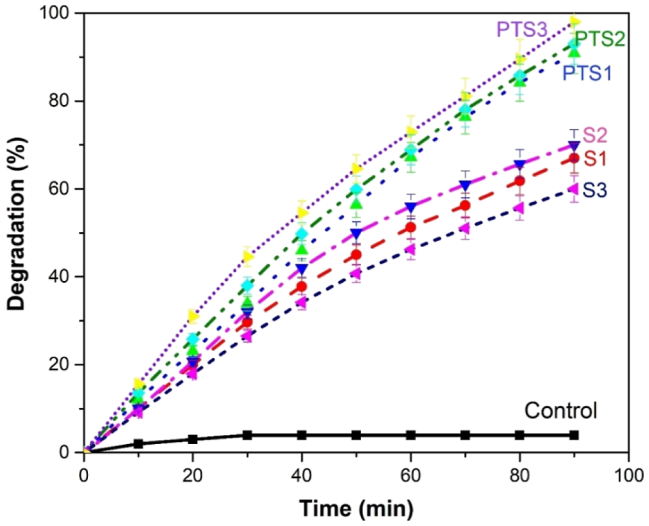

Figure 12. Degradation with respect to time of pristine and MWP-modified MNPs.

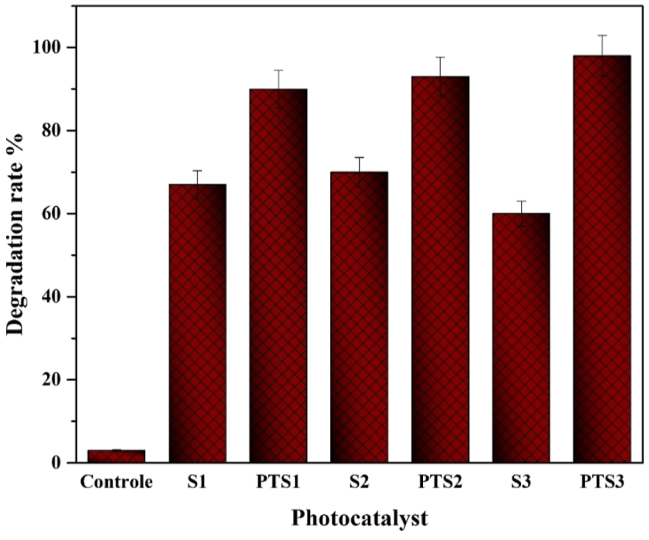

Figure 13. Degradation of RhB dye by using pristine and MWP-modified MNPs.

achieved 76% degradation efficiency against methyl orange dye. These reports suggest that only Das et al.[43] achieved 95% dye degradation efficiency with Mn−ZnO nanoparticles. The plasma synthesis process was the key to the high degradation efficiency of the photocatalyst. None of these investigators studied the effect of the XRD intensity ratio of plasma-treated photocatalysis. The intensity ratio of MNPs, in our study, decreased after the MNPs were exposed to the MWP of oxygen gas. The nanoflower-like structures of MNPs with an increased surface area were seen in plasma-treated samples. The plasma oxidation and sputtering effects caused a reduction in nanoflower size and an increase in reactive surface area. The maximum degradation efficiency of the pristine MNPs was noted at 80%, which increased to 96% after plasma treatment.

Photocatalytic Stability and Reusability. There are many factors to be considered for the success of photocatalysis, including the catalyst cost, reusability, and efficiency. It will add economic value to the process if a catalyst can be retrieved, repurposed, and reutilized without losing its mass or photocatalytic activity. A strong magnetic field, centrifugation, and filtration are the methods used for postprocess recovery of the photocatalyst. This study used external magnetic field and centrifugation methods to recover the photocatalyst from the treated solution for reuse in the next degradation cycles. Four degradation cycles were performed with the same photocatalyst, as shown in Figure 14. In this case, PTS3 was chosen to perform the stability test, since this catalyst produced maximum dye degradation efficiency. After each cycle, the nanoparticles were washed with deionized water and given heat treatment for 2 h at 90 °C. The degradation efficiency after the first cycle was noted as 96%, which reduced to 92% after four degradation cycles. Some weight loss was also noticed at the end of four cycles due to incomplete recovery, washing, and heating of the photocatalyst after each cycle. The tested photocatalyst still exhibits good catalytic activity. A comparison of pre- and postdye degradation XRD patterns of PTS3 photocatalyst are shown in Figure 15. No changes were observed in the XRD patterns except some depression in the intensity peaks after the degradation test, verifying better stability of the catalyst. A small decrease in peak intensities suggests a slight change in the crystallinity of the photocatalyst, which is likely due to photocorrosion and the deposition of dye molecules on the catalyst surface.[48]

CONCLUSIONS

A sol−gel self-combustion method was used to produce $NiFe_2O_4$, $ZnFe_2O_4$, and $NiZnFe_2O_4$ ferrites for MWP treatment and onward use in the photodegradation of organic dyes. The plasma treatment improved the physical, magnetic, and photocatalytic properties of the MNPs. Both pristine and plasma-modified samples exhibited the same structures but notably different morphology, size, band gap and reactive surface area. The photocatalytic activity improved with plasma treatment. The prepared samples showed cubic crystallization. The lattice parameters and crystallite sizes increased after plasma treatment. The peak intensity ratio of (220), (311), and (422), (440) diffraction peaks was used to estimate the cation distributions. The plasma-treated nanoparticles showed slightly different cation distributions from pristine nanoparticles with a decreased peak intensity ratio. After plasma treatment, SEM and Zetasizer analyses showed that MNPs have a large reactive surface area. The large nanoflowers convert to small nanoflowers due to of sputtering phenomenon

https://doi.org/10.1021/acsomega.3c06883
ACS Omega 2024, 9, 14791−14804

Table 5. Comparison of Photocatalytic Activity of This Work with the Published Literature

catalyst	synthesize method	light source	plasma treatment	activity		ref
				untreated	plasma treated	
ZnO	spray pyrolysis	UV-light	treated	MB 50%	MB, 60%	Nam and Boo[40]
$MnFe_2O_4$	sol−gel	UV-light	treated	MB 74%	MB, 91%	Naz et al.[22]
Cu−TiO_2	sol−gel	sunlight	treated	RR-198, 76%	RR-198, 85%	Pandiyaraj et al.[41]
TiO_2	sol−gel	UV-lamp	treated	MG, 75%	MG, 75%	Zolfaghari et al.[42]
Mn−ZnO	sol−gel	xenon lamp	treated	MB, 82%	MB, 95%	Das et al.[43]
TiO_2	co-precipitation	UV-lamp	treated	MG, 72%	MG, 72%	Khaledian et al.[44]
$Mg_{0.5}Ni_{0.5}AlFe_2O_4$	sol−gel	sunlight	untreated	DB, 129 88%		Atrak et al.[45]
$MgFe_2O_4$	solution combustion	sunlight	untreated	MB, 69%		Nguyen et al.[46]
$NiAlFe_2O_4$	co-precipitation	xenon lamp	untreated	MO, 76%		Lassoued et al.[47]

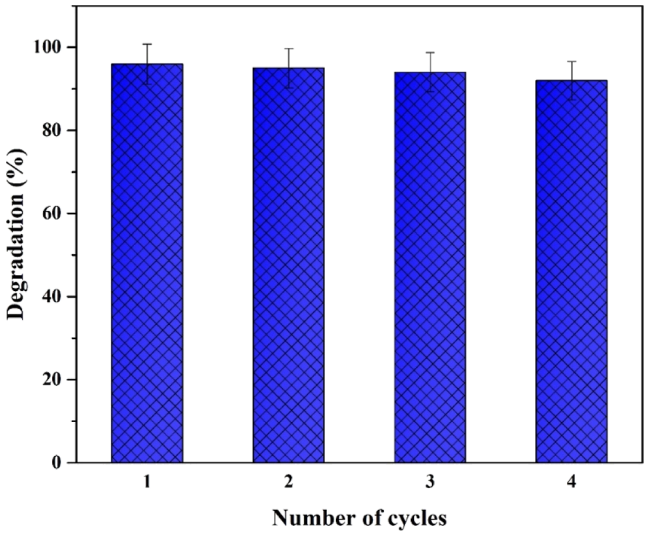

Figure 14. Reusability test of pristine and MWP-modified MNPs.

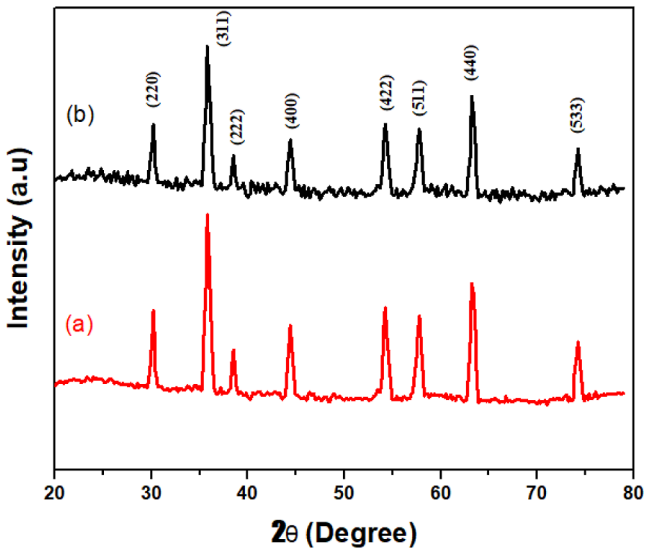

Figure 15. Comparison of pre- and postdye degradation XRD patterns of PTS3 photocatalyst: (a) before dye degradation and (b) after dye degradation.

under plasma exposure. The saturation magnetization of S1 sample increased from 47.5 to 58.9 emu/g, S2 sample from 31.22 to 48.71 emu/g and S3 sample from 33.9 to 52.76 emu/g after plasma treatment. The band gap energy of optimized sample S3 slightly increased from 1.88 to 1.98 eV after plasma exposure but it was still lower than the band gap of other samples. The optimized sample S3 showed high degradation efficiency of 98% against RhB after plasma treatment, which is 38% higher than the pristine photocatalyst.

■ ASSOCIATED CONTENT

Data Availability Statement

The data that supports the findings of this study are available within the article.

■ AUTHOR INFORMATION

Corresponding Author

Shazia Shukrullah − *Department of Physics, University of Agriculture Faisalabad, Faisalabad 38040, Pakistan;* orcid.org/0000-0002-4474-3768; Email: zshukrullah@gmail.com

Authors

Muhammad Aqib Busharat − *Department of Physics, University of Agriculture Faisalabad, Faisalabad 38040, Pakistan*

Muhammad Yasin Naz − *Department of Physics, University of Agriculture Faisalabad, Faisalabad 38040, Pakistan*

Yasin Khan − *Department of Electrical Engineering, College of Engineering, King Saud University, Riyadh 11362, Saudi Arabia*

Ahmed Ahmed Ibrahim − *Department of Physics and Astronomy, College of Science, King Saud University, 11451 Riyadh, Saudi Arabia*

Abdulrehman Ali Al-Arainy − *Department of Electrical Engineering, College of Engineering, King Saud University, Riyadh 11362, Saudi Arabia*

Muhammad Shoaib − *School of Mathematics and Physics, University of Science and Technology, Beijing 100083, China*

Complete contact information is available at: https://pubs.acs.org/10.1021/acsomega.3c06883

Notes

The authors declare no competing financial interest.

■ ACKNOWLEDGMENTS

This work was supported by the Researchers Supporting Project number (RSPD2024R985), King Saud University, Riyadh, Saudi Arabia.

■ REFERENCES

(1) Junaid, M.; Khan, M. A.; Abubshait, S. A.; Akhtar, M. N.; Kattan, N. A.; Laref, A.; Asif Javed, H. M. Structural, spectral, dielectric and magnetic properties of indium substituted copper spinel ferrites

https://doi.org/10.1021/acsomega.3c06883
ACS Omega 2024, 9, 14791−14804

synthesized via sol-gel technique. *Ceram. Int.* **2020**, *46* (17), 27410−27418.
(2) Lisjak, D.; Mertelj, A. Anisotropic magnetic nanoparticles: A review of their properties, syntheses and potential applications. *Prog. Mater. Sci.* **2018**, *95*, 286−328.
(3) Cao, X.; Zhang, B.; Zhao, F.; Feng, L. Synthesis and properties of MPEG-coated superparamagnetic magnetite nanoparticles. *J. Nanomater.* **2012**, *2012* (2), 1−6.
(4) Godbole, R.; Rao, P.; Alegaonkar, P. S.; Bhagwat, S. Influence of fuel to oxidizer ratio on LPG sensing performance of $MgFe_2O_4$ nanoparticles. *Mater. Chem. Phys.* **2015**, *161*, 135−141.
(5) Li, M.; Guo, Q.; Chen, L.; Li, L.; Hou, H.; Zhao, Y. Microstructure and properties of graphene nanoplatelets reinforced AZ91D matrix composites prepared by electromagnetic stirring casting. *J. Mater. Res. Technol.* **2022**, *21*, 4138−4150.
(6) Tezuka, K.; Kogure, M.; Shan, Y. J. Photocatalytic degradation of acetic acid on spinel ferrites MFe_2O_4 (M = Mg, Zn, and Cd). *Catal. Commun.* **2014**, *48*, 11−14.
(7) Zu, Y.; Zhao, Y.; Xu, K.; Tong, Y.; Zhao, F. Preparation and comparison of catalytic performance for nano $MgFe_2O_4$, GO-loaded $MgFe_2O_4$ and GO-coated $MgFe_2O_4$ nanocomposites. *Ceram. Int.* **2016**, *42* (16), 18844−18850.
(8) Yin, Y.; Huo, N.; Liu, W.; Shi, Z.; Wang, Q.; Ding, Y.; Zhang, J.; Yang, S. Hollow spheres of $MgFe_2O_4$ as anode material for lithium-ion batteries. *Scr. Mater.* **2016**, *110*, 92−95.
(9) Kang, D.; Yu, X.; Ge, M.; Song, W. One-step fabrication and characterization of hierarchical $MgFe_2O_4$ microspheres and their application for lead removal. *Microporous Mesoporous Mater.* **2015**, *207*, 170−178.
(10) Singh, S.; Atri, A. K.; Qadir, I.; Sharma, S.; Manhas, U.; Singh, D. Role of Different Fuels and Sintering Temperatures in the Structural, Optical, Magnetic, and Photocatalytic Properties of Chromium-Containing Nickel Ferrite: Kinetic Study of Photocatalytic Degradation of Rhodamine B Dye. *ACS Omega* **2023**, *8* (7), 6302−6317.
(11) Das, P.; Dutta, A.; Bhaumik, A.; Mukhopadhyay, C. Heterogeneous ditopic $ZnFe_2O_4$ catalyzed synthesis of 4H-pyrans: further conversion to 1,4-DHPs and report of functional group interconversion from amide to ester. *Green Chem.* **2014**, *16* (3), 1426−1435.
(12) Sickafus, K. E.; Hughes, R. Spinel compounds: structure and property relations. *J. Am. Ceram. Soc.* **1999**, *82* (12), 3277−3278.
(13) Mathew, D. S.; Juang, R. S. An overview of the structure and magnetism of spinel ferrite nanoparticles and their synthesis in microemulsions. *Chem. Eng. J.* **2007**, *129* (1−3), 51−65.
(14) Cruz-Franco, B.; Gaudisson, T.; Ammar, S.; Bolarin-Miro, A. M.; Sanchez de Jesus, F.; Mazaleyrat, F.; Nowak, S.; Vazquez-Victorio, G.; Ortega-Zempoalteca, R.; Valenzuela, R. Magnetic properties of nanostructured spinel ferrites. *IEEE Trans. Magn.* **2014**, *50* (4), 1−6.
(15) Starko, I.; Tatarchuk, T.; Bououdina, M. La-doped $Ni_{0.5}Co_{0.5}Fe_2O_4$ nanoparticles: effect of cobalt precursors on structure and morphology. *Mol. Cryst. Liq. Cryst.* **2018**, *674*, 110−119.
(16) Song, Z.; Han, D.; Yang, M.; Huang, J.; Shao, X.; Li, H. Formic acid formation via direct hydration reaction ($CO+H_2O\rightarrow HCOOH$) on magnesia-silver composite. *Appl. Surf. Sci.* **2023**, *607*, 155067.
(17) Yang, D.; Wang, Y.; Chen, C.; Su, Y.; Li, L.; Miao, L.; Gu, H.; Zhao, W.; Ding, L.; Hu, D. Oriented Plate-like $KNbO_3$ Polycrystals: Topochemical Mesocrystal Conversion and Piezoelectric and Photocatalytic Responses. *Inorg. Chem.* **2023**, *62* (26), 10408−10419.
(18) Madhukara Naik, M.; Bhojya Naik, H.; Nagaraju, G.; Vinuth, M.; Vinu, K.; Viswanath, R. Green synthesis of zinc doped cobalt ferrite nanoparticles: Structural, optical, photocatalytic and antibacterial studies. *Nano-Struct. Nano-Objects* **2019**, *19*, 100322.
(19) Zhang, Y.; Zhao, M.; Huang, J.; Zhao, N.; Yu, H. Controllable Synthesis, Photocatalytic Property, and Mechanism of a Novel POM-Based Direct Z-Scheme Nano-Heterojunction α-Fe_2O_3/P_2Mo_{18}. *Molecules* **2023**, *28* (18), 6671.
(20) Zheng, Y.; Liu, Y.; Guo, X.; Chen, Z.; Zhang, W.; Wang, Y.; Tang, X.; Zhang, Y.; Zhao, Y. Sulfur-doped g-C_3N_4/rGO porous nanosheets for highly efficient photocatalytic degradation of refractory contaminants. *J. Mater. Sci. Technol.* **2020**, *41*, 117−126.
(21) Zahi, S.; Hashim, M.; Daud, A. R. Synthesis, magnetic properties and microstructure of Ni-Zn ferrite by sol-gel technique. *J. Magn. Magn. Mater.* **2007**, *308* (2), 177−182.
(22) Naz, M. Y.; Irfan, M.; Shukrullah, S.; Ahmad, I.; Ghuffar, A.; Niazi, U. M.; Rahman, S.; Jalalah, M. S.; Alsaiari, M. A.; Khan, M. K. A. Study of structural, magnetic and optical properties of oxygen plasma-treated manganese-doped iron oxide photocatalyst for wastewater treatment. *Appl. Phys. A: Mater. Sci. Process.* **2021**, *127* (7), 491.
(23) Munir, M. A.; Naz, M. Y.; Shukrullah, S.; Ansar, M. T.; Abbas, G.; Makhlouf, M. M. Microwave plasma treatment of NiCuZn ferrite nanoparticles: a novel approach of improving opto-physical and magnetic properties. *Appl. Phys. A: Mater. Sci. Process.* **2022**, *128* (4), 345.
(24) Kumar, G.; Kotnala, R. K.; Shah, J.; Kumar, V.; Kumar, A.; Dhiman, P.; Singh, M. Cation distribution: a key to ascertain the magnetic interactions in a cobalt substituted Mg-Mn nanoferrite matrix. *Phys. Chem. Chem. Phys.* **2017**, *19* (25), 16669−16680.
(25) Singhal, S.; Chandra, K. Cation distribution and magnetic properties in chromium-substituted nickel ferrites prepared using aerosol route. *J. Solid State Chem.* **2007**, *180* (1), 296−300.
(26) Hua, M.; Xu, L.; Cui, F.; Lian, J.; Huang, Y.; Bao, J.; Qiu, J.; Xu, Y.; Xu, H.; Zhao, Y.; et al. Hexamethylenetetramine-assisted hydrothermal synthesis of octahedral nickel ferrite oxide nanocrystallines with excellent supercapacitive performance. *J. Mater. Sci.* **2018**, *53*, 7621−7636.
(27) Andhare, D. D.; Jadhav, S. A.; Khedkar, M. V.; Somvanshi, S. B.; More, S. D.; Jadhav, K. M. Structural and chemical properties of $ZnFe_2O_4$ nanoparticles synthesised by chemical co-precipitation technique. *J. Phys.: Conf. Ser.* **2020**, *1644* (1), 012014.
(28) Wu, L.; Wu, T.; Mao, M.; Zhang, M.; Wang, T. Electrospinning synthesis of Ni°, Fe° codoped ultrafine-$ZnFe_2O_4$/C nanofibers and their properties for lithium ion storage. *Electrochim. Acta* **2016**, *194*, 357−366.
(29) Ambrus, Z.; Balázs, N.; Alapi, T.; Wittmann, G.; Sipos, P.; Dombi, A.; Mogyorósi, K. Synthesis, structure and photocatalytic properties of Fe (III)-doped TiO_2 prepared from $TiCl_3$. *Appl. Catal., B* **2008**, *81* (1−2), 27−37.
(30) Takagahara, T.; Takeda, K.; Takeda, K. Theory of the quantum confinement effect on excitons in quantum dots of indirect-gap materials. *Phys. Rev. B: Condens. Matter Mater. Phys.* **1992**, *46* (23), 15578−15581.
(31) Busharat, M. A.; Naz, M. Y.; Shukrullah, S.; Zahid, M. Post-synthesis Microwave plasma treatment effect on magnetization and morphology of manganese-iron oxide nanoparticles. *Arch. Metall. Mater.* **2021**, *67* (3), 837−842.
(32) Padmapriya, G.; Manikandan, A.; Krishnasamy, V.; Jaganathan, S. K.; Antony, S. A. Spinel $Ni_xZn_{1-x}Fe_2O_4$ ($0.0 \leq x \leq 1.0$) nanophotocatalysts: synthesis, characterization and photocatalytic degradation of methylene blue dye. *J. Mol. Struct.* **2016**, *1119*, 39−47.
(33) Mathubala, G.; Manikandan, A.; Arul Antony, S.; Ramar, P. Enhanced photocatalytic activity of spinel $Cu_xMn_{1-x}Fe_2O_4$ nanocatalysts for the degradation of methylene blue dye and opto-magnetic properties. *Nanosci. Nanotechnol. Lett.* **2016**, *8* (5), 375−381.
(34) Wang, Y.; Jing, Y.; Che, S.; Li, Y.; Xu, Z.; Tang, X. Comparison of magnetic properties of low-temperature-fired NiCuZn ferrites under low-and high-Bi_2O_3 doping modes. *J. Electron. Mater.* **2020**, *49*, 3325−3331.
(35) Yang, Y.; Zhang, H.; Li, J.; Xu, F.; Gan, G.; Wen, D. Effects of Bi_2O_3-Nb_2O_5 additives on microstructure and magnetic properties of low-temperature-fired NiCuZn ferrite ceramics. *Ceram. Int.* **2018**, *44* (9), 10545−10550.
(36) Shirsath, S. E.; Assadi, M. H. N.; Zhang, J.; Kumar, N.; Gaikwad, A. S.; Yang, J.; Maynard-Casely, H. E.; Tay, Y. Y.; Du, J.; Wang, H.; et al. Interface-Driven Multiferroicity in Cubic $BaTiO_3$-$SrTiO_3$ Nanocomposites. *ACS Nano* **2022**, *16* (9), 15413−15424.

https://doi.org/10.1021/acsomega.3c06883
ACS Omega 2024, 9, 14791−14804

(37) Buzea, C.; Pacheco, I. I.; Robbie, K. Nanomaterials and nanoparticles: sources and toxicity. *Biointerphases* **2007**, *2* (4), MR17−MR71.
(38) Shirsath, S. E.; Cazorla, C.; Lu, T.; Zhang, L.; Tay, Y. Y.; Lou, X.; Liu, Y.; Li, S.; Wang, D. Interface-Charge Induced Giant Electrocaloric Effect in Lead Free Ferroelectric Thin-Film Bilayers. *Nano Lett.* **2020**, *20* (2), 1262−1271.
(39) Van Dijken, A.; Meulenkamp, E. A.; Vanmaekelbergh, D.; Meijerink, A. Identification of the transition responsible for the visible emission in ZnO using quantum size effects. *J. Lumin.* **2000**, *90* (3−4), 123−128.
(40) Nam, S. H.; Boo, J. H. Enhancement of photocatalytic activity of synthesized ZnO nanoparticles with oxygen plasma treatment. *Catal. Today* **2016**, *265*, 84−89.
(41) Pandiyaraj, K. N.; Vasu, D.; Ghobeira, R.; Tabaei, P. S. E.; De Geyter, N.; Morent, R.; Pichumani, M.; Padmanabhanan, P. V. A.; Deshmukh, R. R. Dye wastewater degradation by the synergetic effect of an atmospheric pressure plasma treatment and the photocatalytic activity of plasma-functionalized Cu-TiO_2 nanoparticles. *J. Hazard. Mater.* **2021**, *405*, 124264.
(42) Zolfaghari, P.; Khaledian, H. R.; Aliasgharlou, N.; Khorram, S.; Karimi, A.; Khataee, A. Facile surface modification of immobilized rutile nanoparticles by non-thermal glow discharge plasma: Effect of treatment gases on photocatalytic process. *Appl. Surf. Sci.* **2019**, *490*, 266−277.
(43) Das, A.; Sahoo, R. K.; Kumar Mishra, D.; Singh, S. K.; Mane, R. S.; Kim, K. H. Thermal plasma-inspired synthesis of $ZnO_{1-X}Mn_x$ dilute magnetic semiconductors for enhanced visible light photocatalysis. *Appl. Surf. Sci.* **2019**, *467−468*, 1059−1069.
(44) Khaledian, H. R.; Zolfaghari, P.; Elhami, V.; Aghbolaghy, M.; Khorram, S.; Karimi, A.; Khataee, A. Modification of immobilized titanium dioxide nanostructures by argon plasma for photocatalytic removal of organic dyes. *Molecules* **2019**, *24* (3), 383.
(45) Atrak, K.; Ramazani, A.; Taghavi Fardood, S. Eco-friendly synthesis of $Mg_{0.5}Ni_{0.5}Al_xFe_{2-x}O_4$ magnetic nanoparticles and study of their photocatalytic activity for degradation of direct blue 129 dye. *J. Photochem. Photobiol., A* **2019**, *382*, 111942.
(46) Nguyen, L. T.; Nguyen, L. T.; Manh, N. C.; Quoc, D. N.; Quang, H. N.; Nguyen, H. T. T.; Nguyen, D. C.; Bach, L. G. A facile synthesis, characterization, and photocatalytic activity of magnesium ferrite nanoparticles via the solution combustion method. *J. Chem.* **2019**, *2019*, 1−8.
(47) Lassoued, A.; Lassoued, M. S.; Dkhil, B.; Ammar, S.; Gadri, A. Substituted effect of Al^{3+} on structural, optical, magnetic and photocatalytic activity of Ni ferrites. *J. Magn. Magn. Mater.* **2019**, *476*, 124−133.
(48) Ilango, I.; Susanna, D.; Gabriella, R.; Balakrishnan, R. M.; Ettiyappan, J. P. Zinc-decorated barium oxide nanorods for the effective sunlight-induced catalytic degradation of Irgalite violet dye. *Nanotechnol. Environ. Eng.* **2023**, *8* (3), 655−673.

https://doi.org/10.1021/acsomega.3c06883
ACS Omega 2024, 9, 14791−14804